NEW DESIGN RULES OF COLD-FORMED HIGH STRENGTH STEEL CHS-to-RHS X-JOINTS

Madhup Pandey*,[1] and Ben Young[2]

[1]*Department of Civil Engineering, University of Nottingham, Nottingham, United Kingdom*
[2]*Department of Civil and Environmental Engineering, The Hong Kong Polytechnic University, Hong Kong, China*

Abstract

Numerical investigation and design of cold-formed high strength steel (CFHSS) X-joints with circular hollow section (CHS) braces as well as square and rectangular hollow section (SHS and RHS) chords are presented in this paper. The steel grades of hollow section members were S900 and S960 with nominal 0.2% proof stresses of 900 and 960 MPa, respectively. The static performances of CHS-to-RHS X-joints were experimentally investigated by the authors. Accurate finite element (FE) models were developed in this study by duly validating the test results, including ultimate capacities, load-deformation histories and failure modes. A comprehensive FE parametric study was then performed using the verified FE models, where the validity ranges of critical geometric parameters were extended beyond the current threshold limits specified in international codes. The nominal strengths predicted from design rules given in European code and *Comité International pour le Développement et l´Etude de la Construction Tubulaire* (CIDECT) were compared with the ultimate capacities of test and finite element (FE) X-joint specimens. All test and FE X-joint specimens were failed by chord face failure mode and a combination of chord face and chord side wall failure mode, which was termed as a combined failure mode in this investigation. It has been demonstrated that the European code and CIDECT design provisions are unsuitable and uneconomical for the design of cold-formed S900 and S960 steel grades CHS-to-RHS X-joints investigated in this study. As a result, user-friendly, economical and reliable design rules are proposed in this study for the investigated joints.

Keywords: Design proposals; High performance steel; Hollow section members; Numerical investigation; Tubular joints.

*Corresponding author. (e-mail: madhup.pandey@nottingham.ac.uk).

1. Introduction

Primarily, two conventional configurations of tubular joints are popular, first, when both brace and chord members are made of square and/or rectangular hollow section (SHS and RHS) members, i.e. RHS-to-RHS, and second, when both brace and chord members are made of circular hollow section (CHS) members, i.e. CHS-to-CHS. The RHS-to-RHS joint configuration is popular due to simplicity in its fabrication, while the CHS-to-CHS joint configuration is popular due to its low drag coefficient and smaller hydrodynamic loads. The joint configuration studied in this investigation included CHS braces and SHS as well as RHS chords (here onwards, RHS will include SHS), i.e. CHS-to-RHS. The CHS-to-RHS X-joint configuration is the hybrid combination of RHS-to-RHS and CHS-to-CHS X-joint configurations and combines the merits of both the conventional configurations. It is worth mentioning that tubular X-joints can be seen in various structures, including building frames, tubular scaffoldings, tubular racks, trusses, transmission towers, cranes, spatial lattice structures, offshore structures and so on. It is important to note that CHS-to-RHS joints are being used in the manufacture of equipment and structural systems in the road transport and agricultural industries [1]. In addition, CHS-to-RHS configuration has also been used in the Toki Poutangata bridge in New Zealand [2], as shown in Fig. 1.

High strength steel (HSS) (in this study, referred to steels with steel grades higher than S460) hollow section members are in high demand in various civil engineering and infrastructure projects because of their superior strength per unit weight, high toughness, improved weldability, reduced handling cost and erection time. However, the lack of adequate research work and design recommendations are the primary reasons hampering the widespread use of HSS welded tubular structures. Nonetheless, some studies have recently been conducted to investigate the structural performance of HSS tubular stub columns, columns, beam-columns and joints [3-15].

Currently, many international codes [16-18] and guidelines [19-21] permit the application of tubular joints up to S460 steel grade. However, EC3 [22] has allowed the application of tubular joints up to S700 steel grade. It is worth noting that the original formulations of design rules of tubular joints given in codes [16-18] and guidelines [19-21] were based on the experimental, analytical and numerical studies conducted on tubular joints made of S355 and lower steel grades. The extensions of design provisions for steel grades higher than S355 were obtained by simply multiplying the existing design rules with a material factor (C_f). As a result, the suitability of current design rules of tubular joints remains questionable for steel grades exceeding S700, which in turn formed the basis of the investigation and design presented in this paper. Therefore, comprehensive numerical investigation and design of cold-formed S900 and S960 steel grades CHS-to-RHS X- and non-90° X-joints are presented in this paper.

Furthermore, to the best of the authors' knowledge, no other research work is available on CFS CHS-to-RHS X- and non-90° X-joints made of steel grades exceeding S700, except for the experimental investigations carried out by Pandey and Young [9,10]. The test results, including joint ultimate capacities, load-deformation curves and failure modes, were used to develop accurate finite element (FE) models in this study. Subsequently, an extensive FE parametric study was performed using the verified FE models. The nominal strengths predicted from design rules given in EC3 [18] and CIDECT [21] were compared with the ultimate capacities (N_f) of CHS-to-RHS X- and non-90° X-joint test and FE specimens. The current design rules given in EC3 [18] and CIDECT [21] have been demonstrated to be unsuitable and uneconomical for the range of CHS-to-RHS X- and non-90° X-joints investigated in this study. Therefore, economical and reliable design rules are proposed in this study to predict the N_f of cold-formed S900 and S960 steel grades CHS-to-RHS X- and non-90° X-joints. The predictions from the proposed design rules are relatively accurate and less dispersed compared to the predictions obtained from current design rules given in EC3 [18] and CIDECT [21].

2. Details of test programs on cold-formed high strength steel X- and non-90° X-joints

Pandey and Young [9,10] carried out test programs to investigate the ultimate capacities (N_f) and load-deformation behaviour of cold-formed high strength steel (CFHSS) X-joints, where braces and chords were made of CHS and RHS members, respectively. The braces and chords were welded using fully robotic metal active gas welding. In total, 18 tests were conducted, where test specimens were axially compressed through braces. The angles between brace and chord members (θ_1) were 30°, 50°, 70° and 90°. In addition, chord ends were not welded to end plates and were freely deformed during the tests. The thermo-mechanically controlled processed plates of S900 and S960 steel grades were cold-formed to obtain hollow section members. Fig. 2 presents various notations used for CHS-to-RHS non-90° X-joint, which are also valid for 90° X-joint. The static behaviour of CHS-to-RHS X- and non-90° X-joints primarily depend on non-dimensional geometric parameters, including β (d_1/b_0), τ (t_1/t_0), 2γ (b_0/t_0) and h_0/t_0. In Fig. 2, symbols b, h, t and R represent the cross-section width, depth, thickness and external corner radius of RHS members, respectively. The symbol d represents the diameter of the CHS brace. The subscripts 0 and 1 denote chord and brace, respectively. In the test programs [9,10], β varied from 0.59 to 0.89, τ varied from 0.66 to 0.99, 2γ varied from 20.5 to 30.5 and h_0/t_0 varied from 15.3 to 25.5.

The global buckling of brace members was averted by keeping their length (L_H) equal to twice the brace diameter from the heel location of X-joint. The material properties of tubular members and welding material used in the tests of CFHSS X- and non-90° X-joints are summarised in Pandey and Young [23,24]. The measured static yield strengths (i.e. 0.2% proof stresses) of tubular members ranged from 910 to 1059 MPa, while the measured static yield strength of welding filler material was 965 MPa. The failure modes identified in the tests [9,10] were chord face failure (F) and a combination of chord face failure and chord side wall failure mode, named as combined failure (F+S) mode. The test results were obtained in the form of N vs u and N vs v curves, where N, u and v respectively stand for static load, chord face indentation and chord side wall deformation. It should be noted that N vs u curves were used to determine the ultimate capacities (N_f) of X- and non-90° X-joints. The testing machine was paused for 120 seconds at two different locations for each test. The load drops captured during the pauses were used to convert a test curve into a static curve. Consequently, the obtained test results were free from the influence of the applied strain rate. The details of test programs and test results are given in Pandey and Young [9,10].

3. Numerical investigation

3.1. Development of CHS-to-RHS X- and non-90° X-joints finite element models

3.1.1. Introduction

ABAQUS [25] was used to perform comprehensive finite element (FE) analyses in this study. The static (general) analysis procedure given in ABAQUS [25] was used as the solver. As induced strains in FE models due to applied loads were unidirectional in nature, the isotropic strain hardening law was used for the analysis. The von-Mises yield criterion is generally the default criterion used to predict the onset of yielding in most metals, except for porous metals. Therefore, the yielding onsets of FE models in this study were based on the von-Mises yield theory. In FE analyses, the growth of the time step was kept non-linear to reduce the overall computation time. Furthermore, the default Newton-Raphson method was used to find the roots of non-linear equilibrium equations. In addition to the accuracy associated with the Newton-Raphson method, one of the popular benefits of using this numerical technique is its quadratic convergent approach, which in turn significantly increases the convergence rate of non-linear problems.

The material non-linearity was considered in the FE models by assigning the measured values of static stress-strain curves of different regions of the tubular member in the plastic material definition part of the FE model. However, the experimentally obtained constitutive material curves were transformed into true stress-strain curves prior to their inclusion in the FE models. On the other hand, the geometric non-linearities in FE models were considered by enabling the non-linear geometry parameter (*NLGEOM) in ABAQUS [25], which in turn allowed FE specimens to undergo large displacement during the numerical analyses. Furthermore, various parameters, including through-thickness division, contact interactions, mesh seed spacing, corner region extension and element types, were also studied and discussed in the following sub-sections of this paper. Fig. 3 presents typical CHS-to-RHS X-joint FE specimens modelled in this study. The labelling of parametric FE specimens was kept identical to the label system used in the test programs [9,10].

3.1.2. Element type, meshing and mechanical properties

Except for weld parts, all other parts of FE models were developed using second-order hexahedral elements, particularly the C3D20 elements. On the other hand, the second-order tetrahedral element, C3D10, was used to model the weld parts due to their complicated shapes. The weld parts were freely meshed using the free-mesh algorithm, while brace and chord parts were meshed using the structure-mesh algorithm. The use of solid elements helped in making realistic fusions between tubular and weld parts of FE models. Convergence studies were conducted using different mesh sizes, and finally, chord and brace members were seeded at 4 mm and 7 mm intervals, respectively, along both longitudinal and transverse directions. Moreover, the seeding intervals of weld parts reciprocated the seeding spacings of their respective brace parts. In order to assure the smooth transfer of stresses from flange to web regions, corner portions of RHS members were split into ten elements. FE analyses were also conducted to examine the influence of divisions along the wall thickness (t) of tubular members. The results of these FE analyses demonstrated the trivial influence of wall thickness divisions on the load-deformation curves of the investigated X-joints. The use of the C3D20 element as well as the small thickness of test specimens, lead to such observations. It is worth noting that a similar observation was also noticed in other studies [26-28]. Thus, for the validation of FE models, the wall thickness of tubular members was kept undivided.

The test specimens in the experimental programs [9,10] were fabricated from tubular members that belonged to the same batch of tubes used in other investigations carried out by Pandey and Young [11-15,23,24]. On the other hand, Pandey and Young [24] investigated the mechanical properties of welding filler material. The material properties of welding filler material and tubular members can be referred to Pandey and Young [23,24]. The inclusion of static stress-strain curves in FE models helped avert the impact of loading rate from FE results. The true stress-strain curves of flat, corner and curved portions of tubular members and welding filler material were allocated to the corresponding parts of the FE specimens. In this study, the influence of cold-working in RHS members was included in FE models by assigning wider corner regions. Various distances for corner extension in RHS members were considered in the sensitivity analyses, and finally, the corner portions were elongated by $2t$ into the neighbouring flat portions, which was in agreement with other studies conducted on CFHSS tubular members and joints [27-30].

3.1.3. Contact interaction and modelling of weld parts

Two types of interactions were defined in FE models, first, brace-chord interaction, and second, weld-tubular member interaction. Both these types of interactions were established using the built-in surface-to-surface contact definition. The interactions were kept frictionless, and along the normal direction, ‘hard’ contact pressure overclosure was used. In addition, finite sliding was permitted between the interaction surfaces. The interaction surfaces between brace-chord members as well as weld-tubular members were connected to each other using the ‘master-slave’ algorithm technique. This technique permits the separation of fused surfaces under tension, however, it does not allow penetration of fused surfaces under compression. This technique of fusion between various parts of FE models has been successfully used in several other investigations [27,28,31-33]. For the brace-chord interaction, the cross-section surfaces of braces connected to chord members were assigned as ‘master’ regions (relatively less deformable), while both the top and bottom chord connecting surfaces were assigned as ‘slave’ regions (relatively more deformable). Similarly, for weld-tubular member tie connection, the weld surfaces were assigned as the ‘master’ regions (relatively less deformable), while the connecting brace and chord surfaces were assigned as the ‘slave’ regions (relatively more deformable). Fig. 4 presents the contact interactions between weld and tubular members.

The fillet welds were modelled in all FE specimens using the average values of measured weld dimensions reported in Pandey and Young [9,10]. Fig. 5 presents the weld models for typical cases of CHS-to-RHS X-joints covered in this investigation. The inclusion of weld geometries and weld material properties considerably improved the overall accuracies of FE results. In addition, modelling of weld parts helped attain realistic load transfer, particularly for CHS-to-RHS X-joints with $\beta > 0.80$, which in turn facilitated in obtaining the rational joint behaviour. The selection of the C3D10 element maintained optimum stiffness around the joint perimeter due to its ability to take complicated shapes.

3.1.4. Boundary conditions

In order to assign boundary conditions in FE models, two reference points were created. The top and bottom reference points (TRP and BRP) were created at the cross-section centre of brace members, as shown in Fig. 3. Subsequently, TRP and BRP were coupled to their respective brace end cross-section surfaces using kinematic coupling. In order to exactly replicate the test setup, all degrees of freedom (DOFs) of TRP were restrained. On the other hand, except for translation along the height of the FE specimen, all other DOFs of BRP were also restrained. Moreover, all DOFs of other nodes of the FE specimen were kept unrestrained for rotation and translation. Using the displacement control method, the compression load was then applied at the BRP of the FE model. In addition, the size of the step increment was kept small in order to obtain smooth load vs deformation curves. Following this approach, the boundary conditions and load application in FE analyses were identical to the test program [9,10].

3.1.5. Weld heat affected region (WHAR)

The heat transferred to parent tubular members during the welding process has a considerable impact on the overall behaviour of hollow section joints [10,27,28]. The design rules given in international codes [16-18] and guidelines [19-21] are identical for HSS produced through different methods, namely by adding alloying elements and by various heat treatment techniques. However, it has been reported in some recent studies [10,34-37] that HSS produced by different methods exhibited different extents of softening around the welds. Investigations carried out by Stroetmann et al. [34], Javidan et al. [35] and Amraei et al. [36,37] reported 16% to 32% reductions in the ultimate strengths of S960 steel grade parent materials around the welds. Pandey et al. [27] proposed the definition of weld heat affected region (WHAR), as shown in Fig. 6.

The material properties of WHAR of S960 steel grade tubular members with thicknesses varying from 3 to 6 mm were investigated by Pandey and Young [10]. A reduction ranging from 14% to 32% in the ultimate strengths of the parent metals was reported by Pandey and Young [10] in the first 6 mm distance of the heat affected zone. Fig. 7 presents the spread of WHAR for two typical cases of CHS-to-RHS X-joints. A strength reduction (S_{rl}) model proposed by Pandey et al. [27] for S900 and S960 steel grades tubular joints was used to integrate the material properties of WHAR in the FE models, as illustrated in Fig. 8. The proposed strength reduction model was successfully used to perform the numerical investigation and design of CFHSS T- and TF-joints [27,28]. Therefore, it was also included in this investigation, and accordingly, material properties were assigned to the WHAR of CHS-to-RHS X-joints. The adoption of WHAR appreciably improved the accuracies of FE models and, thus, the numerical results.

3.2. Validations of CHS-to-RHS X- and non-90° X-joints finite element models

All CHS-to-RHS X- and non-90° X-joints FE models were developed using the modelling approaches described in the preceding section of this paper. The test results of CHS-to-RHS X- and non-90° X-joints reported in Pandey and Young [9,10] were used to validate the FE models developed in this study. The FE validations were performed by comparing the ultimate capacities (N_f), load vs deformation curves and failure modes of test and FE specimens. The measured dimensions of tubular members and welds were used to develop all FE models. In addition, measured material properties of tubular members, welds and WHAR were also included. The ultimate capacities (N_f) of CHS-to-RHS X- and non-90° X-joints test specimens were compared with those predicted from their corresponding FE model (N_{FE}), as shown in Table 1. The mean (P_m) and coefficients of variation (COV) (V_p) of the comparison are 1.01 and 0.020, respectively. It is worth mentioning that both ultimate load and deformation limit load were used to determine the N_f of test and FE specimens, whichever occurred earlier in the load vs chord face indentation curves. The deformation limit load was defined in accordance with CIDECT [21] and taken as the load corresponding to $0.03b_0$ chord face deformation. In addition, load vs deformation curves were compared between typical test and FE specimens, as shown in Figs. 9 and 10 for CHS-to-RHS X- and non-90° X-joints, respectively. Furthermore, Figs. 11 and 12 respectively present comparisons of distinct failure modes between typical CHS-to-RHS X- and non-90° X-joints test and FE specimens. Hence, it has been proved that the validated FE models closely replicated the overall static behaviour of CHS-to-RHS X- and non-90° X-joints, as shown in Table 1 and Figs. 9-12.

3.3. Parametric study of cold-formed high strength steel CHS-to-RHS X- and non-90° X-joints

3.3.1. General

In order to gain a broad understanding of various critical geometric parameters that affect the static performance of CFHSS CHS-to-RHS X- and non-90° X-joints, a comprehensive numerical parametric study was performed using the FE models validated in this study. In total, 384 FE analyses were performed in the parametric study. Following the experimental investigation, the values of θ_1 were kept as 30°, 50°, 70° and 90° in the FE parametric study. The validity ranges of important geometric ratios were purposefully widened compared to the present limitations set by EC3 [18] and CIDECT [21]. Table 2 presents the ranges of various critical parameters considered in this numerical investigation. The parametric study used all FE modelling techniques described earlier in the paper.

3.3.2. Details of parametric finite element specimens

In the numerical investigation, the dimensions of tubular members included practical sizes. Overall, the values of brace diameter (d_1) of parametric FE specimens ranged from 15 mm to 450 mm. However, the values of cross-section width and depth of RHS chords (b_0 and h_0) of parametric FE specimens varied between 50 mm to 500 mm. Moreover, values of the wall thickness of braces and chords (t_1 and t_0) varied between 2 mm to 10 mm. The external corner radii of RHS chords (R_0) conformed to commercially produced HSS members [38]. In this study, R_0 was designed as $2t$ for $t \leq$ 6 mm, $2.5t$ for $6 < t \leq 10$ mm and $3t$ for $t > 10$ mm, which in turn also satisfy the limits detailed in EN 10219-2 [39]. For 90° CHS-to-RHS X-joints, brace and chord lengths (L_1 and L_0) were designed as $2d_1$ and $4h_0+d_1$, respectively. On the other hand, for non-90° CHS-to-RHS X-joints, brace length from heel location (L_H) was designed as $2d_1$, while chord length (L_0) was kept as $3h_0 + h_0 \tan (90\text{-}\theta_1) + d_1/\cos (90\text{-}\theta_1)$. The lengths of braces and chords were identical to those adopted in the test programs [9,10]. For meshing along the longitudinal and transverse directions of RHS members, seedings were approximately spaced at the minimum of [b/30, h/30]. On the other hand, CHS brace members meshed approximately at an interval of d/30. Overall, the adopted mesh sizes of parametric FE specimens varied between 3 mm to 12 mm. On the other hand, the seeding interval of weld parts of parametric FE specimens reciprocated the seeding interval of their corresponding brace parts. For precise replication of RHS curvatures, the corner portions of RHS members were split into ten parts. Likewise, in the validation process, the corner portions of RHS members were elongated by $2t$ into their neighbouring flat portions. For CHS and RHS members with $t \leq 6$ mm, no divisions were made along the wall thickness of the FE models. However, for CHS and RHS members with $t > 6$ mm, the wall thickness of brace and chord members was divided into two layers.

Following the prequalified welding details given in AWS D1.1M [40], the leg size (w) of fillet weld for 90° CHS-to-RHS X-joints was designed as 1.5 times the minimum of t_1 and t_0. On the other hand, welds for non-90° CHS-to-RHS X-joints were designed in compliance with CIDECT [21] and AWS D1.1M [40] recommendations. The weld designs for both 90° and non-90° FE specimens were consistent with the test programs [9,10]. In the parametric study, the material properties of RHS 150×150×6 were assigned to all RHS members, while the material properties of CHS 88.9×4 were assigned to all CHS members. Besides, weld parts of all parametric FE specimens were given the measured material properties of welding filler material. Table 3 presents the measured material properties of RHS 150×150×6, CHS 88.9×4 and welding filling material used in the parametric study, which include Young's modulus (E), 0.2% proof stress and strain ($\sigma_{0.2}$ and $\varepsilon_{0.2}$), ultimate stress and strain (σ_u and ε_u), fracture strain (ε_f) and Ramberg-Osgood parameter (n). On the other hand, the material properties and spread of WHAR were in accordance with the recommendations proposed by Pandey et al. [27].

3.3.3. Observed failure modes of cold-formed high strength steel CHS-to-RHS X- and non-90° X-joints

The experimental [9,10] and numerical investigations showed two types of failure modes. First, the failure of CHS-to-RHS X- and non-90° X-joints by the yielding of chord flange, which was named chord face failure and denoted by the letter 'F' in this study. Second, the failure of CHS-to-RHS X- and non-90° X-joints due to the combination of chord face and chord side wall failure modes, which was called the combined failure mode and denoted by 'F+S' in this study. It is important to note that these failure modes were defined corresponding to N_f, which in turn was computed by combinedly considering the ultimate and $0.03b_0$ limit [21] loads. The same approach was used to determine the N_f in the test programs [9,10]. The test and parametric FE specimens were failed by the F mode, when N_f was predominantly determined using the $0.03b_0$ limit. The applied loads of CHS-to-RHS X- and non-90° X-joints failed by F mode were monotonically increasing. The test and parametric FE specimens were failed by the F mode in this investigation when $0.30 \leq \beta < 0.75$. For test and parametric FE specimens that failed by F+S mode, the load-deformation curves exhibited a clear ultimate load. Additionally, evident deformations of chord flange, chord webs and chord corner regions were noticed in the test and parametric FE specimens failed by F+S mode. The specimens were failed by the F+S mode in this investigation when $0.75 \leq \beta \leq 0.90$. Moreover, none of the test and FE specimens were failed by the global buckling of brace members.

4. Existing design rules given in EC3 [18] and CIDECT [21]

In order to assess the suitability of EC3 [18] and CIDECT [21] design provisions for cold-formed S900 and S960 steel grades CHS-to-RHS X- and non-90° X-joints, the N_f of test and parametric FE specimens were evaluated against the nominal strengths ($N^*_{E,X}$, $N_{E,X}$, $N^*_{C,X}$ and $N_{C,X}$) predicted from these specifications. The measured dimensions and material properties were used to calculate the nominal strengths. The comparison results for F and F+S failure modes are presented in Tables 4 and 5, respectively. The symbols $N^*_{E,X}$ and $N^*_{C,X}$ stand for nominal strengths predicted from EC3 [18] and CIDECT [21] without including the recommended material factors (C_f). On the contrary, the symbols $N_{E,X}$ and $N_{C,X}$ stand for nominal strengths predicted from EC3 [18] and CIDECT [21] by duly including the recommended material factors. The $N_f / N^*_{E,X}$ and $N_f / N^*_{C,X}$ comparisons examined the suitability of design provisions originally developed for S355 or lower steel grades. However, the $N_f / N_{E,X}$ and $N_f / N_{C,X}$ comparisons examined the appropriateness of current EC3 [18] and CIDECT [21] design provisions.

Chord face failure ($\beta \leq 0.85$)

EC3 [18]:

For steel grades up to S355 or below:

$$N^*_{E,X} = \frac{\pi}{4} \frac{k_n f_{y0} t_0^2}{(1-\beta)\sin\theta_1} \left(\frac{2\eta}{\sin\theta_1} + 4\sqrt{1-\beta} \right) / \gamma_{M5} \tag{1}$$

For steel grades higher than S355:

$$N_{E,X} = C_f \left(N^*_{E,X} \right) \tag{2}$$

CIDECT [21]:

For steel grades up to S355 or below:

$$N^*_{C,X} = \frac{\pi}{4} Q_f \frac{f_{y0} t_0^2}{\sin\theta_1} \left(\frac{2\eta}{(1-\beta)\sin\theta_1} + \frac{4}{\sqrt{1-\beta}} \right) \tag{3}$$

For steel grades higher than S355:

$$N_{C,X} = C_f\left(N^*_{C,X}\right) \tag{4}$$

Chord side wall failure (β = *1.0*)

EC3 [18]:

For steel grades up to S355 or below:

$$N^*_{E,X} = \frac{\pi}{4}\frac{k_n f_b t_0}{\sin\theta_1}\left(\frac{2d_1}{\sin\theta_1} + 10t_0\right) / \gamma_{M5} \tag{5}$$

For steel grades higher than S355:

$$N_{E,X} = C_f\left(N^*_{E,X}\right) \tag{6}$$

CIDECT [21]:

For steel grades up to S355 or below:

$$N^*_{C,X} = \frac{\pi}{4}Q_f\frac{f_k t_0}{\sin\theta_1}\left(\frac{2d_1}{\sin\theta_1} + 10t_0\right) \tag{7}$$

For steel grades higher than S355:

$$N_{C,X} = C_f\left(N^*_{C,X}\right) \tag{8}$$

The nominal strengths from EC3 [18] were obtained using 0.2% proof stress and partial safety factor (γ_{M5}) equal to 1.0. On the contrary, CIDECT [21] uses the minimum of yield stress and 0.80 times the respective ultimate stress for joint strength calculation. Unlike EC3 [18], CIDECT [21] uses different values of partial safety factors (γ_M) for different tubular joints, which are given in IIW [19]. However, their effects have already been included in the design provisions given in CIDECT [21]. The nominal strengths from design rules given in CIDECT [21] were calculated using γ_M equal to 1.0 and 1.25 for chord face plastification failure and chord side wall buckling failure, respectively. In Eqs. (1)-(8), chord stress functions are denoted by k_n and Q_f (in this investigation, the values of k_n and Q_f were adopted as 1.0), yield stress of chord member is denoted by f_{y0}, η is equal to d_1/b_0, chord side wall buckling stresses are denoted by f_b and f_k, and angle between brace and chord (θ_1) is in degrees.

5. Reliability analysis

In order to examine the reliability of existing and proposed design equations, a reliability study was performed as per AISI S100 [41]. Eq. (9) was used to calculate the reliability index (β_0). In this investigation, a lower bound value of 2.50 was taken as the target β_0. Therefore, when $\beta_0 \geq 2.50$, the design equation was treated as reliable in this study.

$$\beta_0 = \frac{\ln(C_\phi M_m F_m P_m / \phi)}{\sqrt{V_M^2 + V_F^2 + C_P V_P^2 + V_Q^2}} \quad (9)$$

A dead load (DL)-to-live load (LL) ratio of 0.20 was used to compute the calibration coefficient (C_ϕ) in Eq. (9). For the material factor, the mean value and COV are respectively symbolised by M_m and V_M. For the fabrication factor, the mean value and COV are respectively symbolised by F_m and V_F. Referring to AISI S100 [41], the M_m and V_M were adopted as 1.10 and 0.10, respectively. Additionally, F_m and V_F were adopted as 1.00 and 0.10, respectively. The resistance factor required to convert nominal strength to design strength is denoted by ϕ. The mean value of ratios of test and FE ultimate capacities-to-nominal strengths predicted from code was denoted by P_m, while the corresponding COV was denoted by V_P. The correction factor (C_P) given in AISI S100 [41] was also used in Eq. (9) to incorporate the effect of the number of data under consideration. Besides, V_Q symbolised the COV of load effects. To evaluate the reliability levels of EC3 [18] design provisions, the DL and LL were combined as 1.35DL + 1.5LL as per EN [42], and thus, the calculated value of C_ϕ was 1.463. Further, to examine the reliability levels of CIDECT [21] design provisions as well as the design rules proposed in this study, the DL and LL were combined as 1.2DL + 1.6LL as per ASCE 7 [43], and the calculated value of C_ϕ was 1.521.

6. Comparisons between ultimate capacities and nominal strengths

The summaries of comparisons between N_f and nominal strengths are shown in Tables 4 and 5. In total, 402 data are presented in Tables 4 and 5, including 18 test data [9,10] and 384 parametric FE data generated in this study. The comparisons are also graphically shown in Figs. 13 and 14. Table 4 and Fig. 13 present the comparisons for test and parametric FE specimens that failed by the F mode. In Fig. 13, generally, test and parametric FE specimens with small values of β ratio and large values of 2γ ratio lie below the unit slope line (i.e. y=x). For such specimens, the joint strength corresponding to the $0.03b_0$ limit was insufficient to cause the yielding of the chord flanges. On the contrary, the yield line theory has been used to derive the existing design equation given in EC3 [18] and CIDECT [21] for specimens that failed by the F mode. Hence, N_f of test and parametric FE specimens became smaller than the corresponding nominal strengths predicted from design rules given in EC3 [18] and CIDECT [21]. As a result, such data fall below the line of unit slope. The data above the line of unit slope, on the other hand, indicate test and parametric FE specimens with medium to large values of β ratio and small values of 2γ ratio. The stress-strain behaviour of HSS material is remarkably different to that of mild steel. Prolonged elasticity, progressive yielding, the absence of a yield plateau, and a low ultimate-to-yield stress ratio are all common features of the HSS stress-strain curve [10]. These differences in the stress-strain behaviour could change the deformation extent of chord connecting faces, which in turn could also delay the development of membrane action in the chord flanges.

The summary of comparison results of test and parametric FE specimens that failed by the F+S mode are shown in Table 5 and Fig. 14. The comparison results demonstrated that current EC3 [18] and CIDECT [21] design provisions are quite conservative but have shown large values of COV and also unreliable for $\phi = 1.0$. The data above the unit slope line in Fig. 14 typically represent test and parametric FE specimens with large values of β ratio and small values of 2γ and h_0/t_0 ratios. As the β ratio of test and parametric FE specimens failed by the F+S mode increased, the brace member gradually approached the chord corner regions. Consequently, the N_f of such joints increased because of the enhanced rigidity of the chord corner regions. On the other hand, the corresponding increase in nominal strength predicted from design rules given in current EC3 [18] and CIDECT [21] was lower than the N_f of test and parametric FE specimens. Subsequently, such cases fall above the line of unit slope in Fig. 14.

These comparison results proved that EC3 [18] and CIDECT [21] design provisions are unsuitable for the series of CHS-to-RHS X- and non-90° X-joints studied in this investigation. In addition, existing design rules have shown large values of COV as well as they are not reliable for the recommended value of $\phi = 1.0$.

7. Proposed design rules

Accurate and reliable design rules are proposed in this study for cold-formed S900 and S960 steel grades CHS-to-RHS X- and non-90° X-joints failed by the F and F+S failure modes. The design rules are proposed based on the minimum scatter approach. In addition, the influences of governing geometric parameters on the static structural performance of CHS-to-RHS X- and non-90° X-joints were carefully considered. The validity ranges of critical geometric factors influencing the static structural performance of CHS-to-RHS X- and non-90° X-joints were extended beyond their existing limits given in EC3 [18] and CIDECT [21]. Furthermore, as welds were modelled in all parametric FE specimens, the effects of weld and associated WHAR were implicitly included in the proposed design rules. In order to obtain design strengths (N_d), the proposed nominal strengths (N_{pn}) shall be multiplied by their correspondingly recommended resistance factors (ϕ), i.e. $N_d = \phi$ (N_{pn}).

7.1. CHS-to-RHS X- and non-90° X-joints failed by chord face failure (F) mode

The factors θ_1, β and 2γ demonstrated a significant influence on the static structural performance of CHS-to-RHS X- and non-90° X-joints failed by the F mode. A design equation (see Eq. (10)) is proposed to predict the nominal strength of CFHSS CHS-to-RHS X- and non-90° X-joints failed by the F mode by taking into consideration the effect of important geometric factors as well as P_m and V_p of the overall comparison.

$$N_{pn} = \frac{f_{y0} t_0^2}{(\sin\theta_1)^{(1.8-0.02\theta_1)}} \left[\frac{1.5 e^{3\beta}}{0.65 + 0.025(2\gamma)} \right] \quad (10)$$

The Eq. (10) is valid for $\theta_1 \geq 30°$, $0.30 \leq \beta < 0.75$, $16.6 \leq 2\gamma \leq 50$, $15 \leq h_0/t_0 \leq 50$ and $0.50 \leq \tau \leq 1.0$. The values of P_m and V_p are 1.02 and 0.202, respectively, as shown in Table 4. For Eq. (10), ϕ equal to 0.75 is proposed, resulting in β_0 equal to 2.54. Thus, Eq. (10) must be multiplied by ϕ equal to 0.75 to obtain the design strength (N_d). The comparisons of test and FE strengths vs nominal and proposed strengths are graphically presented in Fig. 13. In addition, the distributions of the ratios of ultimate capacities of test and FE specimens-to-nominal strengths predicted from current and proposed design rules are shown in Fig. 15. Compared with existing design provisions, the predictions from Eq. (10) are relatively more accurate, less dispersed and reliable for the investigated joints failed by the F mode.

7.2. CHS-to-RHS X- and non-90° X-joints failed by combined failure (F+S) mode

The ultimate capacities of test and parametric FE specimens failed by the F+S mode showed significant influence of θ_1, β and 2γ parameters. A design equation (see Eq. (11)) is proposed to predict the nominal strength of CFHSS CHS-to-RHS X- and non-90° X-joints failed by the F+S mode by taking into consideration the effect of important geometric factors as well as P_m and V_p of the overall comparison.

$$N_{pn} = \frac{f_{y0} t_0^2}{(\sin\theta_1)^{1.3}} \left[\frac{65\beta - 35}{0.75 + 0.015(2\gamma)} \right] \tag{11}$$

The Eq. (11) is valid for $\theta_1 \geq 30°$, $0.75 \leq \beta \leq 0.90$, $16.6 \leq 2\gamma \leq 50$, $15 \leq h_0/t_0 \leq 50$ and $\tau = 1$. The values of P_m and V_p are 1.00 and 0.187, respectively, as shown in Table 5. For Eq. (11), ϕ equal to 0.75 is proposed, resulting in β_0 equal to 2.53. Thus, Eq. (11) must be multiplied by ϕ equal to 0.75 to obtain the design strength (N_d). The comparisons of test and FE strengths vs nominal and proposed strengths are graphically presented in Fig. 14. Moreover, the distributions of the ratios of ultimate capacities of test and FE specimens-to-nominal strengths predicted from current and proposed design rules are shown in Fig. 16. Compared with existing design provisions, the predictions from Eq. (11) are relatively more accurate, less dispersed and reliable for the investigated joints failed by the F+S mode.

7.3. Proposed unified design equations

The design equations to predict the ultimate capacities of cold-formed S900 and S960 steel grades CHS-to-RHS T- and TF-joints were proposed by Pandey et al. [27,28]. In order to propose unified design equations, an attempt has been made to keep the formats of the proposed design equations matching between CHS-to-RHS X-, T- and TF-joints failed by identical failure modes. The unified design equations for different observed failure modes are proposed as follows:

- For CFHSS CHS-to-RHS X-, T- and TF-joints failed by chord face failure (F) mode:

$$N_{pn} = \frac{f_{y0} t_0^2}{(\sin\theta_1)^{\mathrm{E}}} \left[\frac{\mathrm{A} e^{\mathrm{D}\beta}}{\mathrm{B} + \mathrm{C}(2\gamma)} \right] \tag{12}$$

- For CFHSS CHS-to-RHS X-, T- and TF-joints failed by combined failure (F+S) mode:

$$N_{pn} = \frac{f_{y0} t_0^2}{(\sin\theta_1)^{\mathrm{E}}} \left[\frac{\mathrm{A}\beta + \mathrm{D}}{\mathrm{B} + \mathrm{C}(2\gamma)} \right] \tag{13}$$

The values of coefficients (A to E) as well as range of β ratio of X-, T- and TF-joints failed by F and F+S failure modes are given in Tables 6 and 7, respectively. It should be noted that a linear interpolation is required between F and F+S failure modes to determine the ultimate capacities of CHS-to-RHS T- and TF-joints.

8. Conclusions

Following are the key conclusions drawn from this investigation:

- The overall accuracy of the finite element (FE) model remarkably improved by using second-order solid elements, modelling of weld parts and particularly the inclusion of corresponding weld heat affected regions.
- The CHS-to-RHS X- and non-90° X-joints investigated in this study were failed by chord face failure (F) mode and a combination of chord face and chord side wall failure mode, i.e. combined failure (F+S) mode.
- The ultimate capacities of CHS-to-RHS X- and non-90° X-joints failed by F mode were governed by the $0.3b_0$ deformation limit criterion. However, the ultimate capacities of CHS-to-RHS X- and non-90° X-joints failed by F+S mode were jointly controlled by the peak load and deformation limit load criteria.
- For the range of CHS-to-RHS X- and non-90° X-joints investigated in this study, EC3 [18] and CIDECT [21] design provisions are found to be unsuitable and uneconomical.
- User-friendly, economical and reliable design equations are proposed to predict the ultimate capacities of cold-formed S900 and S960 steel grades CHS-to-RHS X- and non-90° X-joints.
- The validity ranges of critical geometric parameters used in the proposed design equations exceeded those given in EC3 [18] and CIDECT [21].

- Unified design equations are also proposed to predict the nominal strengths of cold-formed S900 and S960 steel grades CHS-to-RHS X-, T-, TF-joints failed by F and F+S modes.

Acknowledgement

The work described in this paper was fully supported by a grant from the Research Grants Council of the Hong Kong Special Administrative Region, China (Project No. 17210218).

References

[1] Mashiri F.R. and Zhao X.L. Plastic mechanism analysis of welded thin-walled T-joints made up of circular braces and square chords under in-plane bending. Thin-Walled Structures, 2004, 42(5), 759-783.

[2] https://dcstructuresstudio.com/toki-poutangata-pedestrian-bridge/.

[3] Zhong Y and Zhao O. Experimental and numerical studies on post-fire behaviour of S700 high strength steel circular hollow sections under combined compression and bending. Thin-Walled Structures, 2022; 181:110004.

[4] Zhong Y, Su A, and Zhao O. Post-fire local buckling behaviour of cold-formed S700 high strength steel circular hollow sections under axial compression: Experiments, modelling and design. Thin-Walled Structures, 2023; 184:110511.

[5] Zhong Y, Zhao O and Gardner L. Experimental and numerical investigation of S700 high strength steel CHS beam–columns after exposure to fire. Thin-Walled Structures, 2022; 175:109248.

[6] Zhong Y, Sun Y, Zhao O and Gardner L. Structural response and residual capacity of S700 high-strength steel CHS columns after exposure to elevated temperatures. Journal of Structural Engineering (ASCE), 2022; 148(6):04022050.

[7] Zhong Y, Tan KH and Zhao O. Experimental and numerical investigations of S700 high strength steel tubular section stub columns after exposure to elevated temperatures. Thin-Walled Structures, 2021; 163:107669.

[8] Lan X, Wardenier J and Packer JA. Design of chord sidewall failure in RHS joints using steel grades up to S960. Thin-Walled Structures, 2021;163:107605.

[9] Pandey, M. and Young, B. Structural performance of cold-formed high strength steel tubular X-Joints under brace axial compression. Engineering Structures, 2020, 208, 109768.

[10] Pandey, M. and Young, B. Static resistances of cold-formed high strength steel tubular non-90° X-Joints. Engineering Structures, 2021, 239, 112064.

[11] Pandey, M. and Young, B. Post-Fire Behaviour of Cold-Formed High Strength Steel Tubular T- and X-Joints. Journal of Constructional Steel Research, 2021, 186, 106859.

[12] Pandey, M. and Young, B. Ultimate Resistances of Member-Rotated Cold-Formed High Strength Steel Tubular T-Joints under Compression Loads. Engineering Structures, 2021, 244, 112601.

[13] Pandey, M. and Young, B. Stress Concentration Factors of Cold-Formed High Strength Steel Tubular T-Joints. Thin-walled Structures, 2021, 166, 107996.

[14] Pandey, M. and Young, B. Experimental Investigation on Stress Concentration Factors of Cold-formed High Strength Steel Tubular X-Joints. Engineering Structures, 2021, 243, 112408.

[15] Pandey, M. and Young, B. Effect of Member Orientation on the Static Strengths of Cold-Formed High Strength Steel Tubular X-Joints. Thin-walled Structures, 2022, 170, 108501.

[16] AISC 360. Specification for structural steel buildings. ANSI/AISC 360-16, American National Standards Institute and American Institute of Steel Construction, Chicago, 2016.

[17] ISO 14346. Static design procedure for welded hollow-section joints – Recommendations. ISO 14346-2013, British Standard International Standards, Geneva, 2013.

[18] Eurocode 3 (EC3). Design of Steel Structures-Part 1-8: Design of Joints. EN 1993-1-8, European Committee for Standardization, Brussels, Belgium, 2005.

[19] IIW. Static design procedure for welded hollow section joints – Recommendations. IIW Doc. XV-1402-12 and IIW Doc. XV-E-12-433, International Institute of Welding, Paris, 2012.

[20] Packer, J.A. and Henderson, J.E. Hollow Structural Section Connections and Trusses – A Design Guide. Canadian Institute of Steel Construction (CISC), Willowdale, Ontario, 1997.

[21] Packer, J.A., Wardenier, J., Zhao, X.L., van der GJ, Vegte and Kurobane, Y. (2009). Design guide for rectangular hollow section (RHS) joints under predominantly static loading. Comite´ International pour le Developpement et l'Etude de la Construction TuECbulaire (CIDECT), Design Guide No. 3, 2nd edn., LSS Verlag, Dortmund, Germany, 2009.
[22] Eurocode 3 (EC3). Design of steel structures. Part 1-12: Additional rules for the extension of EN 1993 up to steel grades S700. EN 1993-1-12, European Committee for Standardization, Brussels, Belgium, 2007.
[23] Pandey, M. and Young, B. Tests of cold-formed high strength steel tubular T-joints. Thin-Walled Struct, 2019, 143, 106200.
[24] Pandey, M. and Young, B. Compression capacities of cold-formed high strength steel tubular T-joints. J Constr Steel Res, 2019, 162, 105650.
[25] Abaqus/Standard. Version 6.17. USA: K. a. S. Hibbit, 2017.
[26] Crockett, P. Finite element analysis of welded tubular connections. PhD Thesis, University of Nottingham, UK, 1994.
[27] Pandey, M., Chung, K.F. and Young, B. Design of cold-formed high strength steel tubular T-joints under compression loads. Thin-Walled Structures, 2021, 164, 107573.
[28] Pandey, M., Chung, K.F. and Young, B. Numerical investigation and design of fully chord supported tubular T-joints. Engineering Structures, 2021, 239, 112063.
[29] Xu, F., Chen, J. and Chan, T.M. Numerical analysis and punching shear fracture based design of longitudinal plate to concrete-filled CHS connections. Construction and Building Materials, 2017, 156, 91-106.
[30] Liu, H.X., Fang, H., Zhu, J.Y. and Chan, T.M. Numerical investigation on the structural performance of octagonal hollow section columns. Structures, 2021, 34, 3257-3267.
[31] Hu, Y.F., Chung, K.F., Jin, H., Ban, H. and Nethercot, D.A. Structural behaviour of T-joints between high strength S690 steel cold-formed circular hollow sections. Journal of Constructional Steel Research, 2021, 182, 106686.
[32] Becque J. and Cheng S. Sidewall buckling of equal-width RHS truss X-joints. Journal of Structural Engineering, ASCE, 2017;143(2):04016179.
[33] Björk T and Saastamoinen H. Capacity of CFRHS X-joints made of double-grade S420 steel. In Tubular Structures XIV-Proceedings of the 14th International Symposium on Tubular Structures, ISTS, 2012, 167-176.
[34] Stroetmann, R., Kastner, T., Halsig, A. and Mayr, P. Mechanical properties and a new design approach for welded joints at high strength steels. Hong Kong:Engineering Research and Practice for Steel Construction, 2018, 79–90.
[35] Javidan, F., Heidarpour, A., Zhao, X.L., Hutchinson, C.R. and Minkkinen, J. Effect of weld on the mechanical properties of high strength and ultra-high strength steel tubes in fabricated hybrid sections. Engineering Structures, 2016, 118, 16–27.
[36] Amraei, M., Ahola, A., Afkhami, S., Bjork, T., Heidarpour, A. and Zhao, X.L. Effects of heat input on the mechanical properties of butt-welded high and ultra-high strength steels. Engineering Structures, 2019, 198, 109460.
[37] Amraei, M., Afkhami, S., Javaheri, V., Larkiola, J., Skriko, T., Bjork, T. and Zhao, X.L. Mechanical properties and microstructural evaluation of the heat-affected zone in ultra-high strength steels, Thin-Walled Structures, 2020, 157, 107072.
[38] SSAB. Strenx Tube 900 and 960 MH. Data Sheet 2042 and 2043, Sweden, 2017.
[39] Eurocode (EN). Cold formed welded structural hollow sections of non-alloy and fine grain steels-Part 2: Tolerances, dimensions and sectional properties. EN 10219-2-2019, European Committee for Standardization, Brussels, Belgium, 2019.

[40] AWS D1.1M Structural Welding Code – Steel. AWS D1.1/D1.1M-20, American Welding Society (AWS), Miami, 2020.
[41] AISI S100. North American specification for the design of cold-formed steel structural members. AISI S100-16, American Iron and Steel Institute, Washington, DC, 2016.
[42] Eurocode (EN). Eurocode: Basis of structural design. EN 1990 (2002), European Committee for Standardization, Brussels, Belgium, 2002.
[43] ASCE 7. Minimum Design Loads for Buildings and Other Structures. ASCE/SEI 7-16, American Society of Civil Engineers (ASCE), New York, 2016.

(a) Site view of the Toki Poutangata bridge.

(b) CHS-to-RHS K-joint used in the Toki Poutangata bridge.

Fig. 1. CHS-to-RHS joints used in the Toki Poutangata bridge, New Zealand [2].

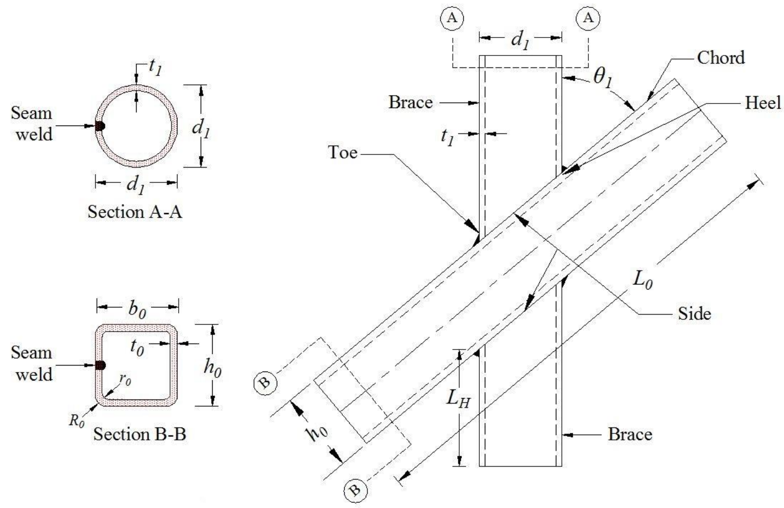

Fig. 2. Definitions of notations for CHS-to-RHS X- and non 90° X-joints.

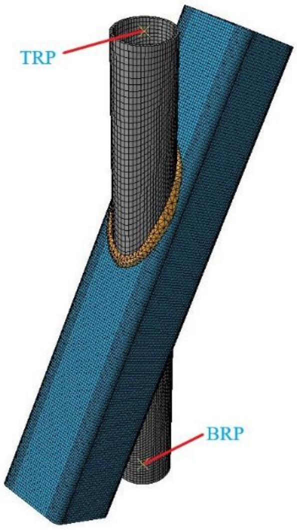

(a) Typical 30° CHS-to-RHS X-joint.

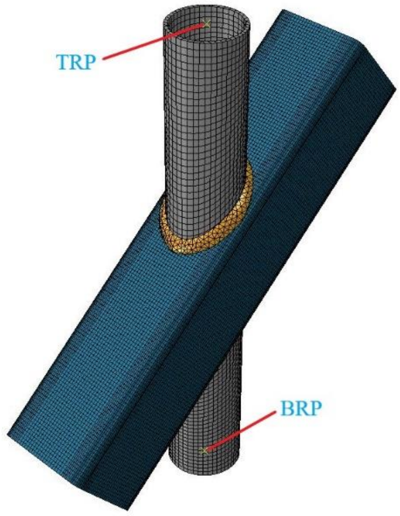

(b) Typical 50° CHS-to-RHS X-joint.

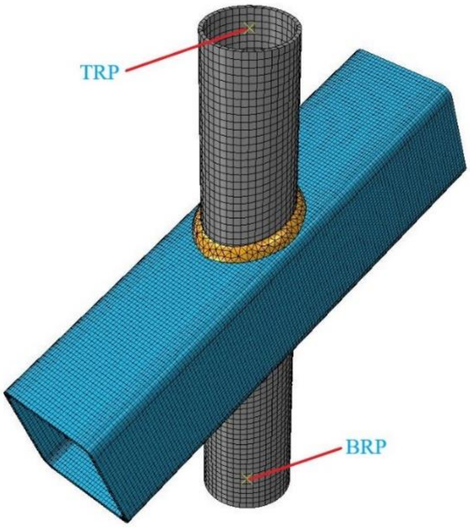

(c) Typical 70° CHS-to-RHS X-joint.

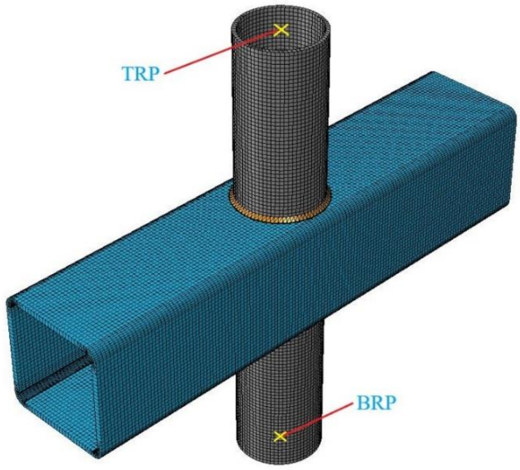

(d) Typical 90° CHS-to-RHS X-joint.

Fig. 3. Typical CHS-to-RHS X- and non 90° X-joints FE models.

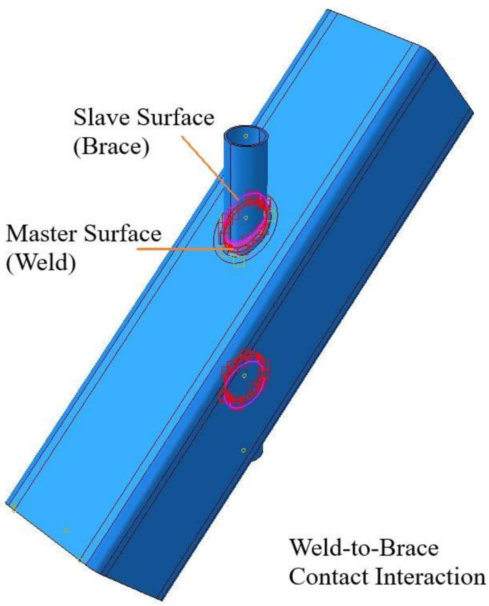

(a) Weld-to-brace contact interaction.

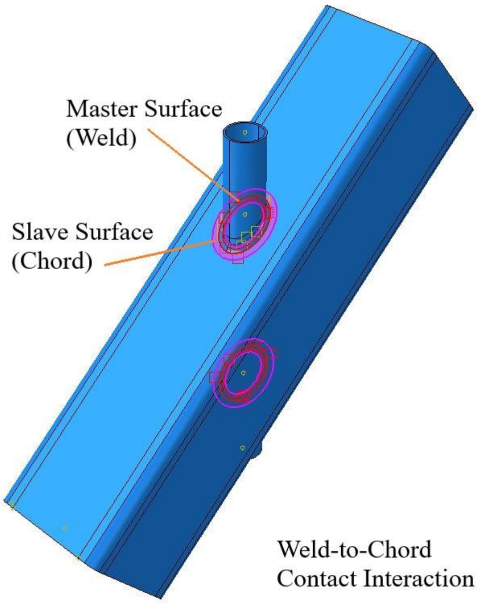

(b) Weld-to-chord contact interaction.

Fig. 4. Weld-tubular member contact interactions.

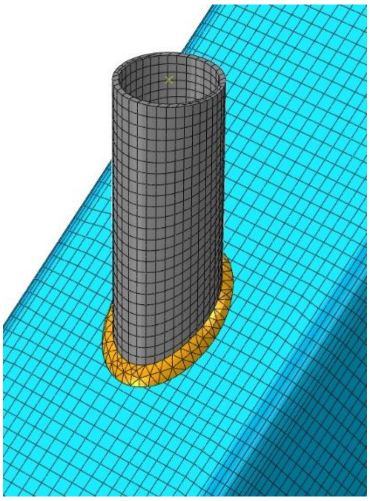

(a) Weld completely falls on the flat region of chord connecting face.

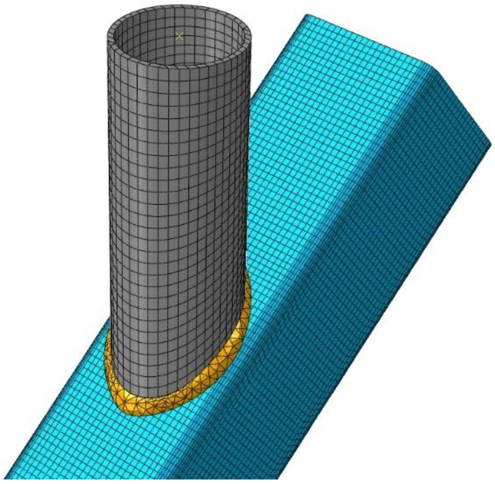

(b) Weld entered the corner region of chord connecting face.

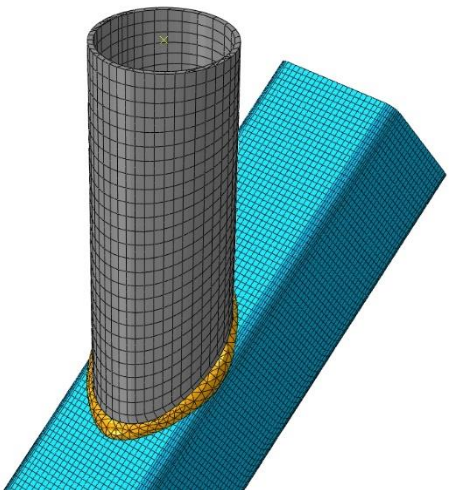

(c) Weld falls on flat and corner regions of chord connecting face.

Fig. 5. Weld modelling for typical cases of CHS-to-RHS X- and non 90° X-joints.

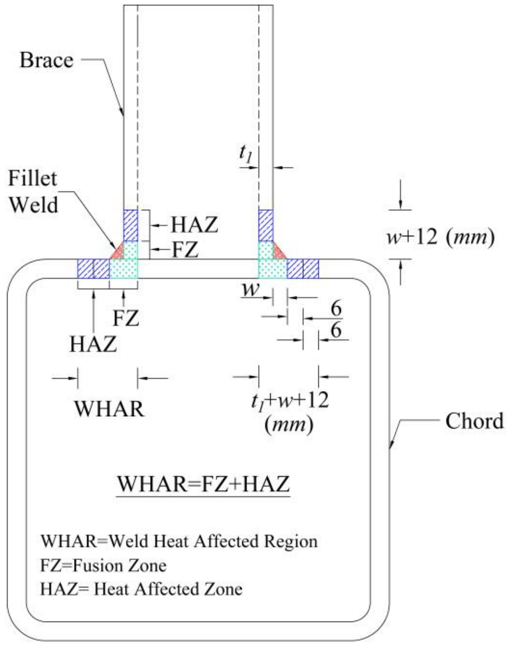

Fig. 6. Definition of weld heat affected region (WHAR) [27].

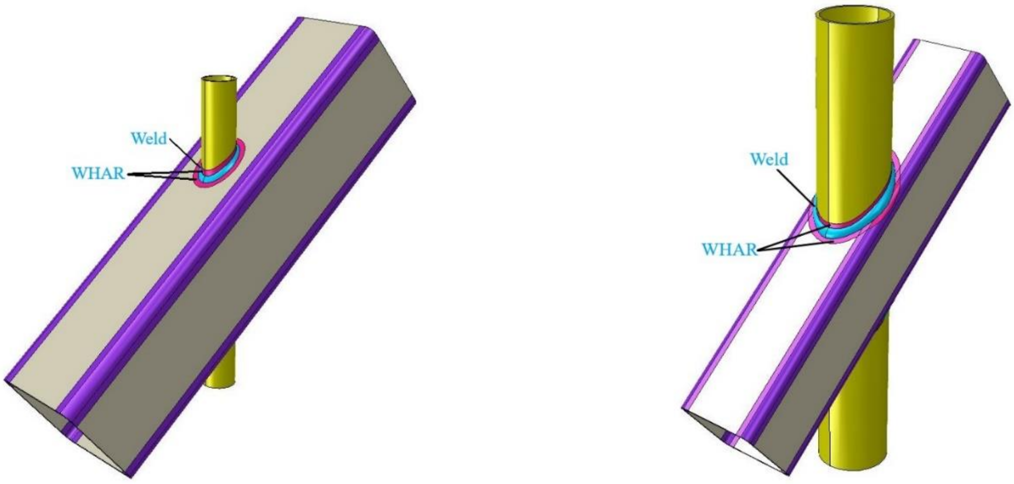

(a) WHAR spread when weld falls completely on the flat region of chord.

(b) WHAR spread when weld falls partially on flat and corner regions of chord.

Fig. 7. Weld heat affected region spread for typical cases of CHS-to-RHS X- and non 90° X-joints.

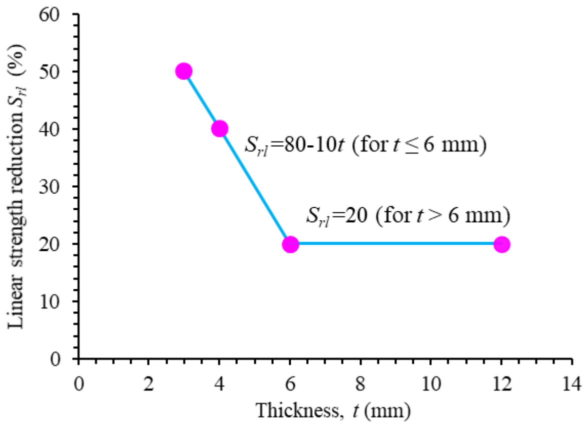

Fig. 8. Linear strength reduction model for WHAR of S900 and S960 steel grades tubular joints [27].

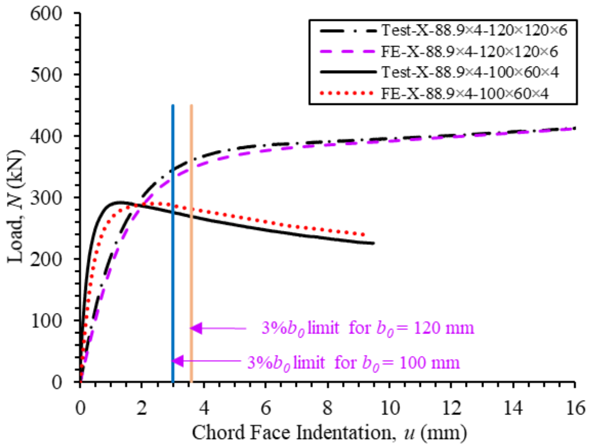

(a) Load vs chord face indentation curves.

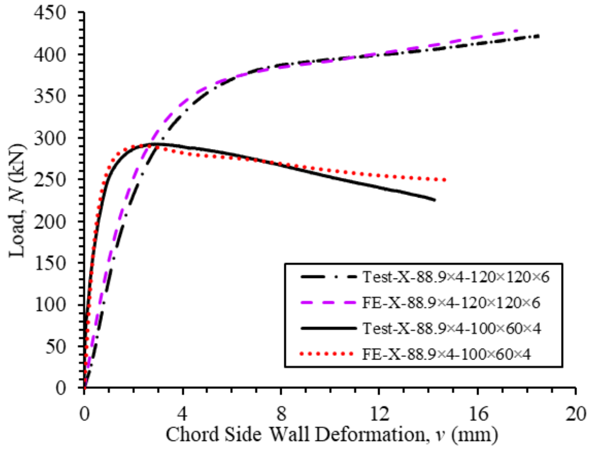

(b) Load vs chord side wall deformation curves.

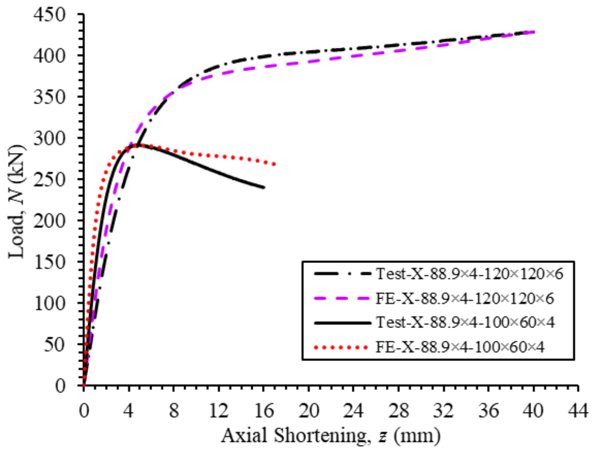

(c) Load vs axial shortening curves.

Fig. 9. Test vs FE load-deformation curves for 90° CHS-to-RHS X-joints.

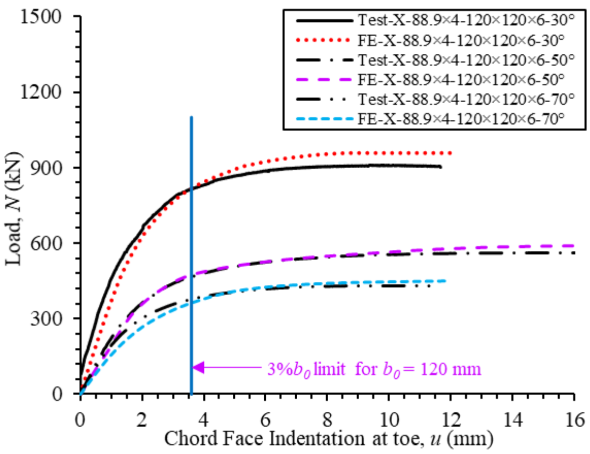

(a) Load vs chord face indentation curves.

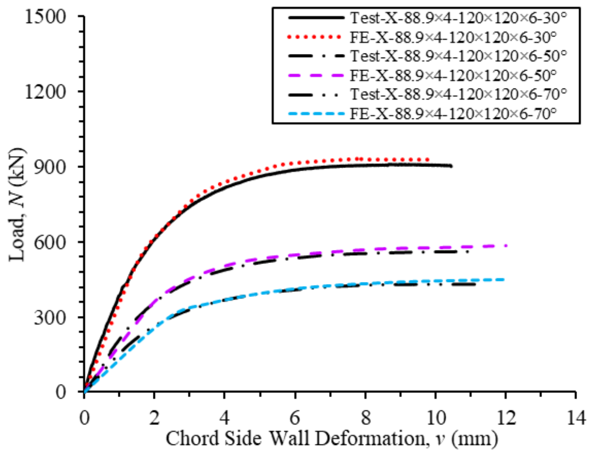

(b) Load vs chord side wall deformation curves.

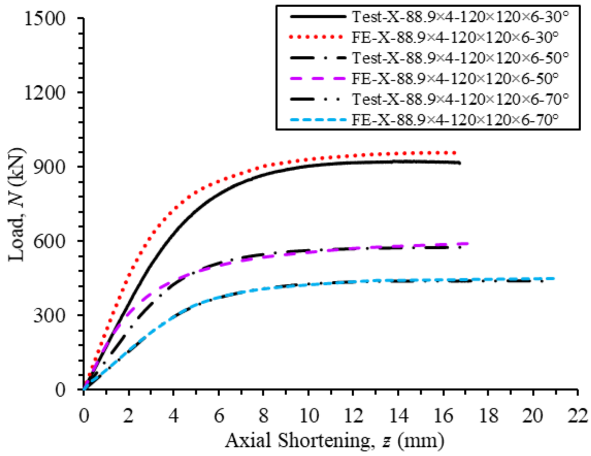

(c) Load vs axial shortening curves.

Fig. 10. Test vs FE load-deformation curves for non-90° CHS-to-RHS X-joints.

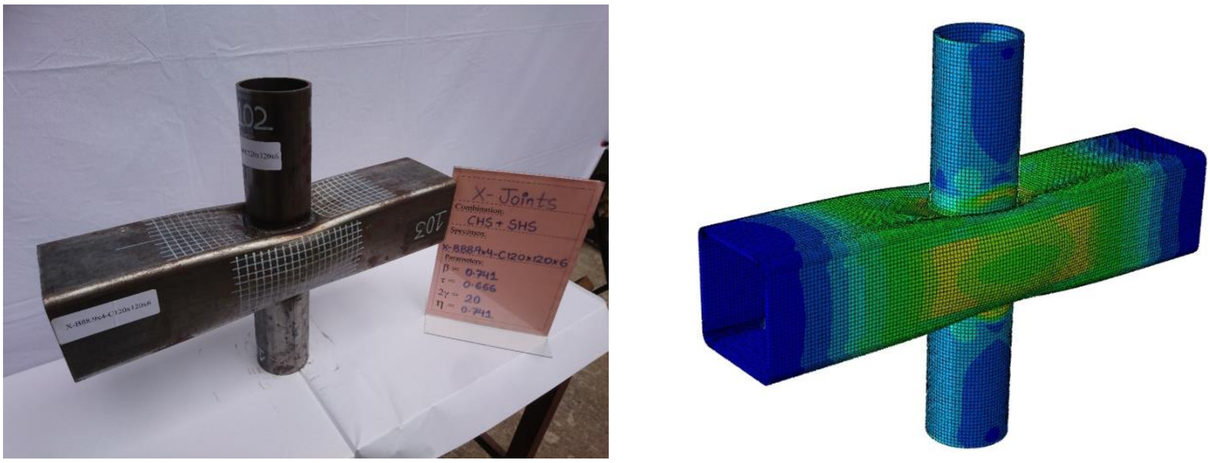

(a) Comparison of test and FE 90° CHS-to-RHS X-joint failed by F mode.

(b) Comparison of test and FE 90° CHS-to-RHS X-joint failed by F+S mode.

Fig. 11. Failure modes comparisons between test and FE 90° CHS-to-RHS X-joints.

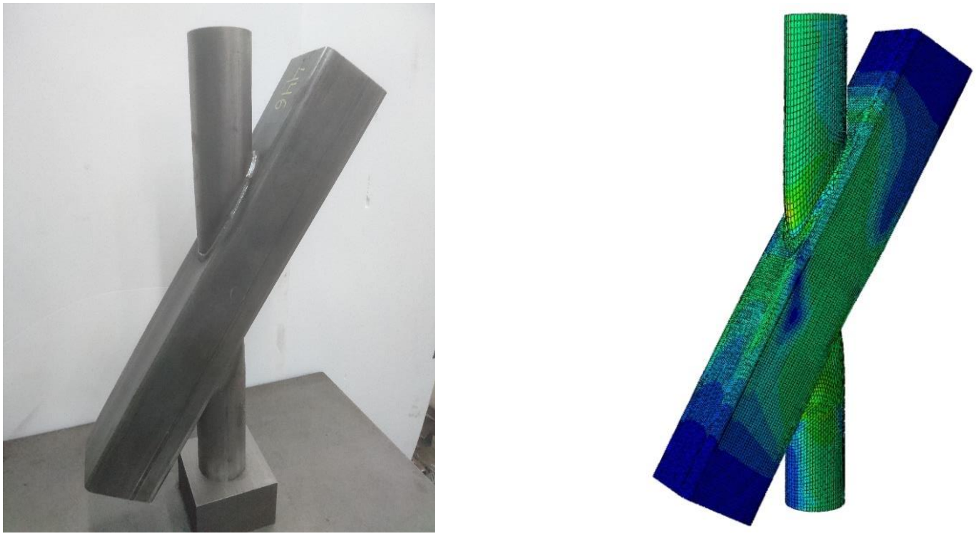

(a) Comparison of test and FE 30° CHS-to-RHS X-joint failed by F mode.

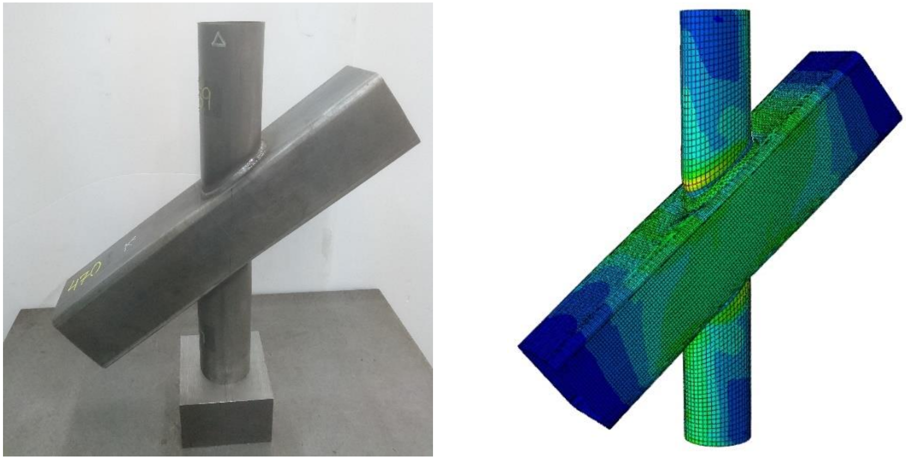

(b) Comparison of test and FE 50° CHS-to-RHS X-joint failed by F mode.

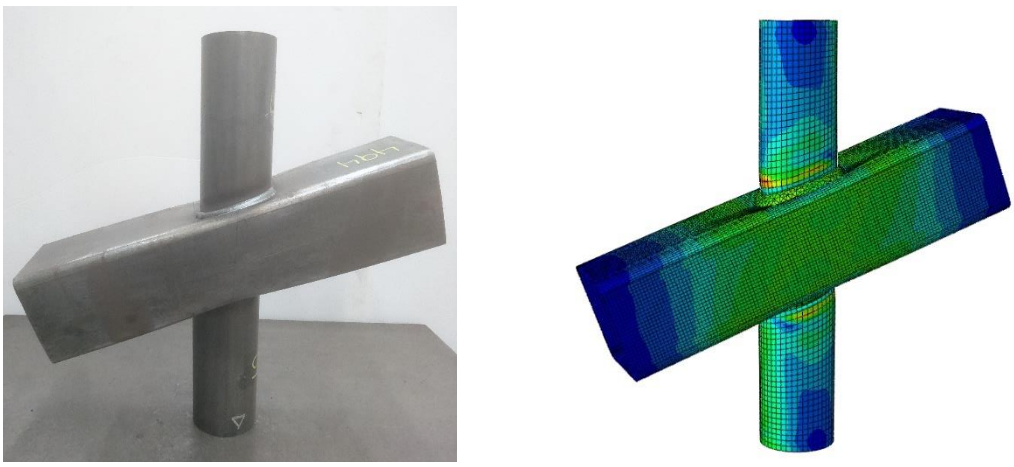

(c) Comparison of test and FE 70° CHS-to-RHS X-joint failed by F mode.

Fig. 12. Comparison between test and FE non-90° CHS-to-RHS X-joints failed F mode.

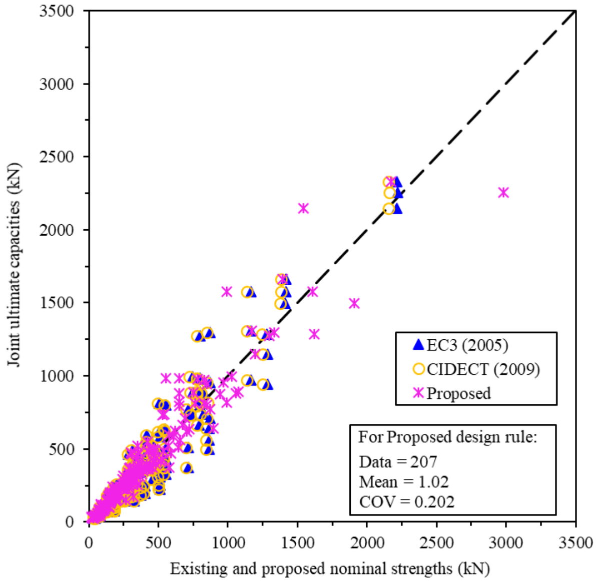

Fig. 13. Comparisons of test and FE ultimate capacities with current and proposed nominal strengths for CHS-to-RHS X-joints failed by F mode.

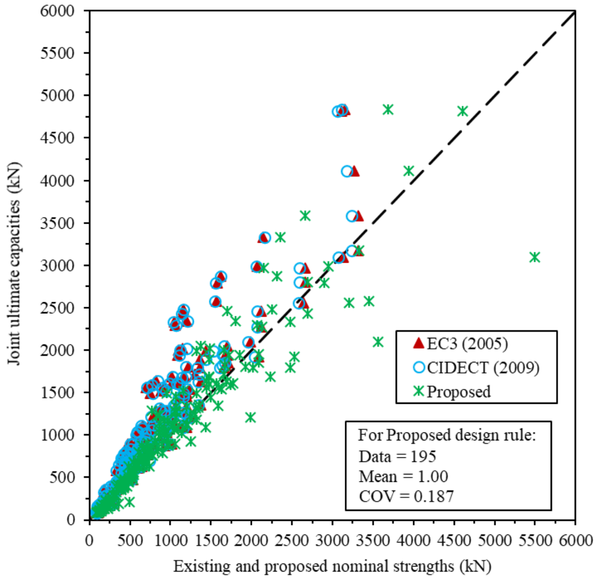

Fig. 14. Comparisons of test and FE ultimate capacities with current and proposed nominal strengths for CHS-to-RHS X-joints failed by F+S mode.

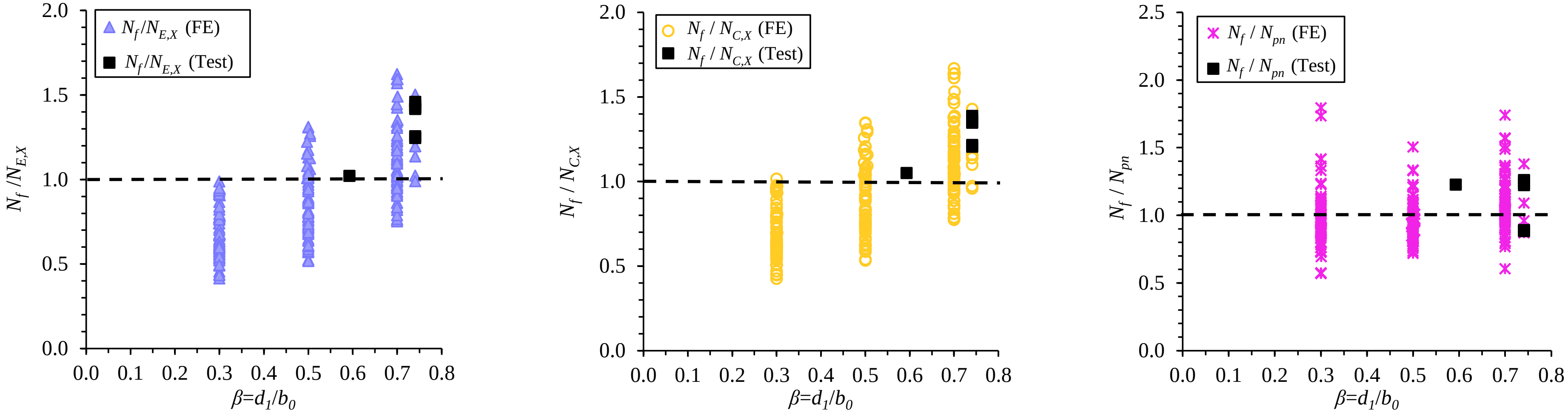

(a) For EC3 [18] (b) For CIDECT [21] (c) For proposed design rule

Fig. 15. Test and FE ultimate capacities-to-current and proposed nominal strengths for CHS-to-RHS X- and non 90° X-joints failed by F mode.

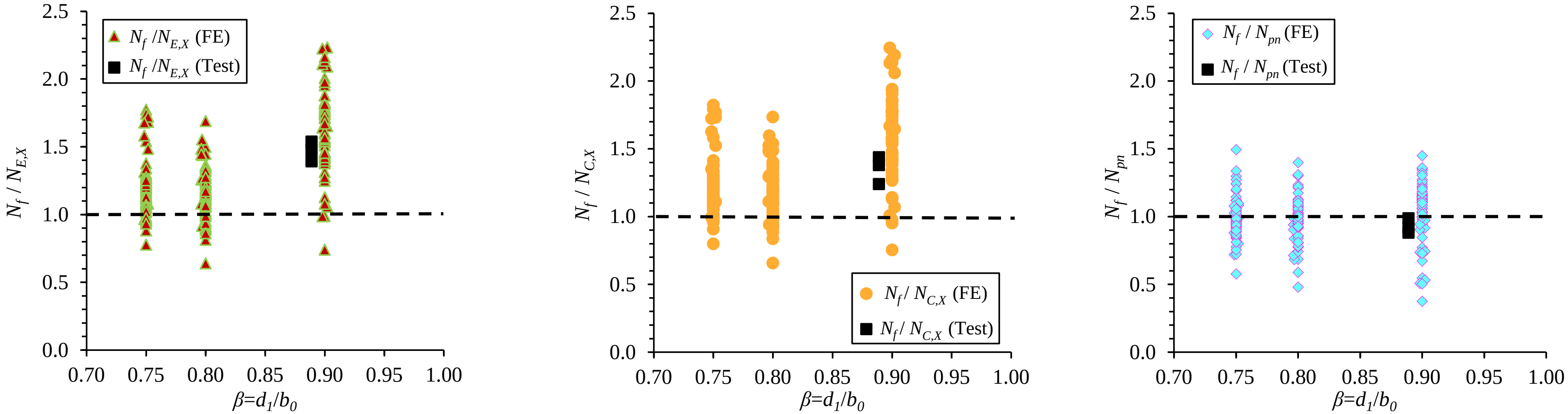

(a) For EC3 [18] (b) For CIDECT [21] (c) For proposed design rule

Fig. 16. Test and FE ultimate capacities-to-current and proposed nominal strengths for CHS-to-RHS X- and non 90° X-joints failed by F+S mode.

Table 1. Test vs FE joint strength comparisons for CHS-to-RHS X- and non 90° X-joints.

Specimens $X\text{-}d_1{\times}t_1\text{-}b_0{\times}h_0{\times}t_0$	β	Failure modes	Test Strengths (kN) N_f	FE Strengths (kN) N_{FE}	$\frac{N_f}{N_{FE}}$
X-88.9×4-150×150×6	0.59	F	224.7	213.5	1.05
X-88.9×3-120×60×4	0.74	F	176.7	178.1	0.99
X-88.9×3-120×60×4-R	0.74	F	178.8	178.7	1.00
X-88.9×4-120×60×4	0.74	F	181.4	181.5	1.00
X-88.9×4-120×60×4-R	0.74	F	176.2	179.6	0.98
X-88.9×4-120×120×6	0.73	F	361.6	350.1	1.03
X-88.9×4-120×120×6-R	0.73	F	364.8	355.7	1.03
X-88.9×4-100×60×4	0.89	F+S	292.5	290.5	1.01
X-88.9×4-100×100×4	0.88	F+S	276.4	275.9	1.00
X-88.9×4-100×100×4-R	0.88	F+S	287.9	281.3	1.02
X-88.9×3-120×60×4-30°	0.74	F	361.3	362.1	1.00
X-88.9×4-120×120×6-30°	0.73	F	817.7	820.2	1.00
X-88.9×3-120×60×4-50°	0.74	F	219.3	216.5	1.01
X-88.9×4-120×120×6-50°	0.73	F	486.1	479.3	1.01
X-88.9×4-120×120×6-50°-R	0.73	F	469.1	475.4	0.99
X-88.9×3-120×60×4-70°	0.74	F	200.3	194.1	1.03
X-88.9×3-120×60×4-70°-R	0.74	F	204.1	198.0	1.03
X-88.9×4-120×120×6-70°	0.73	F	379.4	365.6	1.04
				Mean (P_m)	1.01
				COV (V_p)	0.020

Note: F = Chord face failure; F+S = Combined failure.

Table 2. Validity ranges of critical geometric parameters used in parametric study.

Parameters	Validity Ranges
θ_1	[30° to 90°]
β (d_1/b_0)	[0.30 to 0.90]
2γ (b_0/t_0)	[16.6 to 50]
h_0/t_0	[16.6 to 50]
τ (t_1/t_0)	[0.50 to 1.0]

Table 3. Material properties of tubular members and weld used in parametric study.

Materials	Measured Material Properties							
	E (GPa)	$\sigma_{0.2}$ (MPa)	$\varepsilon_{0.2}$ (%)	σ_u (MPa)	$0.8\sigma_u$ (MPa)	ε_u (%)	ε_f (%)	n
RHS (150×150×6)*	208.5	1059.1	0.71	1145.7	916.6	1.48	9.37#	5.31
CHS (88.9×4)*	208.5	1006.7	0.68	1105.3	884.3	1.58	12.26$	9.49
Weld Material@	202.7	965.2	0.68	1023.4	818.7	5.41	17.15$	8.13

Note: * Pandey and Young [23]; @Pandey and Young [24]; #fracture strain based on 50 mm gauge length; $fracture strain based on 25 mm gauge length.

Table 4. Summary of comparisons between test and FE ultimate capacities with existing and proposed nominal strengths for CHS-to-RHS X- and non 90° X-joints failed by F mode.

θ_1	Parameters	Comparisons				
		$\frac{N_f}{N_{E,X}^*}$	$\frac{N_f}{N_{E,X}}$	$\frac{N_f}{N_{C,X}^*}$	$\frac{N_f}{N_{C,X}}$	$\frac{N_f}{N_{pn}}$
30°	No. of data (n)	50	50	50	50	50
	Mean (P_m)	0.71	0.88	0.81	0.90	1.07
	COV (V_p)	0.218	0.218	0.218	0.218	0.242
50°	No. of data (n)	51	51	51	51	51
	Mean (P_m)	0.67	0.84	0.77	0.86	1.00
	COV (V_p)	0.334	0.334	0.331	0.331	0.206
70°	No. of data (n)	51	51	51	51	51
	Mean (P_m)	0.74	0.93	0.85	0.95	1.03
	COV (V_p)	0.309	0.309	0.301	0.301	0.172
90°	No. of data (n)	55	55	55	55	55
	Mean (P_m)	0.77	0.97	0.88	0.98	0.99
	COV (V_p)	0.308	0.308	0.297	0.297	0.177
Overall	No. of data (n)	207	207	207	207	207
	Mean (P_m)	0.73	0.91	0.84	0.93	1.02
	COV (V_p)	0.302	0.302	0.295	0.295	0.202
	Resistance factor (ϕ)	1.00	1.00	1.00	1.00	0.75
	Reliability index (β_0)	0.40	0.96	0.86	1.13	2.54

Table 5. Summary of comparisons between test and FE ultimate capacities with existing and proposed nominal strengths for CHS-to-RHS X- and non 90° X-joints failed by F+S mode.

θ_1	Parameters	Comparisons				
		$\frac{N_f}{N_{E,X}^*}$	$\frac{N_f}{N_{E,X}}$	$\frac{N_f}{N_{C,X}^*}$	$\frac{N_f}{N_{C,X}}$	$\frac{N_f}{N_{pn}}$
30°	No. of data (n)	48	48	48	48	48
	Mean (P_m)	0.92	1.15	1.05	1.17	0.98
	COV (V_p)	0.187	0.187	0.178	0.178	0.266
50°	No. of data (n)	48	48	48	48	48
	Mean (P_m)	1.06	1.32	1.20	1.33	1.00
	COV (V_p)	0.193	0.193	0.179	0.179	0.196
70°	No. of data (n)	48	48	48	48	48
	Mean (P_m)	1.13	1.41	1.27	1.41	1.01
	COV (V_p)	0.251	0.251	0.238	0.238	0.150
90°	No. of data (n)	51	51	51	51	51
	Mean (P_m)	1.13	1.42	1.27	1.41	1.00
	COV (V_p)	0.247	0.247	0.238	0.238	0.113
Overall	No. of data (n)	195	195	195	195	195
	Mean (P_m)	1.06	1.33	1.20	1.33	1.00
	COV (V_p)	0.239	0.239	0.226	0.226	0.187
	Resistance factor (ϕ)	1.00	1.00	1.00	1.00	0.75
	Reliability index (β_0)	1.53	2.17	2.04	2.35	2.53

Table 6. Values of coefficients for proposed chord face failure unified design equation.

Joint Types	β range	Coefficients A	B	C	D	E
CHS-to-RHS X- and non 90° X-joints	$0.30 \leq \beta < 0.75$	1.5	0.65	0.025	3	$1.8\text{-}0.02\theta_1$
CHS-to-RHS T-Joint [27]	$0.30 \leq \beta \leq 0.70$	1.2	0.6	0.025	3.1	0^*
CHS-to-RHS TF-Joint [28]	$0.30 \leq \beta \leq 0.74$	1.25	0.5	0.03	3.3	0^*

Note: * non-90° T- and TF-joints were not investigated by Pandey et al. [27,28].

Table 7. Values of coefficients for proposed combined failure unified design equation.

Joint Types	β range	Coefficients A	B	C	D	E
CHS-to-RHS X- and non 90° X-joints	$0.75 \leq \beta \leq 0.90$	65	0.75	0.015	-35	1.3
CHS-to-RHS T-Joint [27]	$0.73 \leq \beta \leq 0.90$	57	0.80	0.013	-30	0^*
CHS-to-RHS TF-Joint [28]	$0.75 \leq \beta \leq 0.90$	70	0.70	0.013	-40	0^*

Note: * non-90° T- and TF-joints were not investigated by Pandey et al. [27,28].